Accepted Manuscript

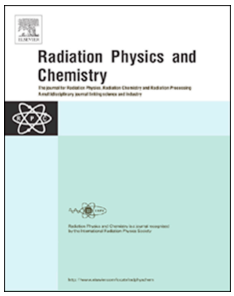

Optimized EDXRF system for simultaneous detection of gold and silver nanoparticles in tumor phantom

M. Santibáñez, R. Saavedra, J. Vedelago, F. Malano, M. Valente

PII: S0969-806X(19)30340-8

DOI: https://doi.org/10.1016/j.radphyschem.2019.108415

Article Number: 108415

Reference: RPC 108415

To appear in: *Radiation Physics and Chemistry*

Received Date: 10 April 2019

Revised Date: 12 June 2019

Accepted Date: 17 July 2019

Please cite this article as: Santibáñez, M., Saavedra, R., Vedelago, J., Malano, F., Valente, M., Optimized EDXRF system for simultaneous detection of gold and silver nanoparticles in tumor phantom, *Radiation Physics and Chemistry* (2019), doi: https://doi.org/10.1016/j.radphyschem.2019.108415.

Optimized EDXRF system for simultaneous detection of gold and silver nanoparticles in tumor phantom

M. Santibáñez[1,2,*], R. Saavedra[1], J. Vedelago[3,4], F. Malano[1,2] and M. Valente[2,3,4]

[1] Departamento de Ciencias Físicas, Universidad de la Frontera, Avda. Francisco Salazar, 01145 Temuco, Chile.
[2] Centro de Física e Ingeniería Aplicada en Medicina (CFIM), Universidad de La Frontera, Temuco, Chile.
[3] Instituto de Física Enrique Gaviola (IFEG), CONICET & FAMAF – Universidad Nacional de Córdoba, Ciudad Universitaria, 5000, Córdoba, Argentina.
[4] Laboratorio de Investigación e Instrumentación en Física Aplicada a la Medicina e Imágenes por Rayos X (LIIFAMIR^{X}), FAMAF - Universidad Nacional de Córdoba, Ciudad Universitaria, 5000, Córdoba, Argentina.

* Corresponding author: mauricio.santibanez@ufrontera.cl

Abstract

An energy-dispersive X-ray fluorescence system (EDXRF) was optimized for simultaneous detection of gold and silver nanoparticles inside water-equivalent phantoms applied to theranostics. The optimization process was carried out in order to maximize the fluorescence detection, keeping dose levels as low as possible. Gold and silver fluorescent emissions were simultaneously detected emerging from phantom's volume, allowing the future development of multi-parametric imaging associated to specific tumor characteristics. For fluorescence detection, gold L_{III}-edge and silver K-edge emission lines were used, exited with a conventional X-ray source with a tungsten target. Several combinations of filters of different thickness were used to hardening the Bremsstrahlung spectrum, thus producing energetically narrow beams with central energy according to both excitation edges. In the case of gold, incident spectrum was optimized by means of strontium (Sr) and yttrium (Y) filters to relatively incrementing photons capable of exciting gold L_{III}-edge, while silver K-edge excitation was improved using a tin (Sn) filter. Filtering combinations made of 212.0 μm Sr with 94.5 μm Sn, and 130.2 μm Y with 94.5 μm Sn maximized fluorescence detection sensitivity and minimized delivered dose, resulting in doses 2.24 and 2.36 times lower than individual gold or silver fluorescent detection. Furthermore, when dual gold and silver fluorescent detection was performed, the minimum detectable concentration was lower than single element detection: 0.042±0.002 mg/mL of Au and 0.024±0.005 mg/mL of Ag in dual detection against 0.058±0.003 mg/mL of Au and 0.124±0.007 mg/mL of Ag when measured independently.

Keywords: gold nanoparticles, silver nanoparticles, tumor biomarkers, targeting radiotherapy, *in vivo* EDXRF.

1. Introduction

Currently, the infusion of high atomic number nanoparticle agents within biological tissue, represents one of the most promising technologies aimed at imaging and therapeutic medical tasks. Among its potentialities, it would offer: tumor markers (Hainfeld et al., 2006; Cheong et al., 2010), real-time monitoring (Manohar et al., 2013; Ricketts et al., 2013; Santibáñez et al., 2017; Wu et al., 2013) and dose enhancement highly localized (Delorme et al., 2017; Hainfeld et al., 2013, 2004; Mattea et al., 2017; Ngwa et al., 2014; Santibáñez et al., 2018; Zhang et al., 2014).

Gold and silver nanoparticles (GNPs and AgNPs) have been studied in detail and functionalized bounding to lipids (Bromma et al., 2019; Yang et al., 2018), peptides (Albertini et al., 2019; Chen et al., 2016; Grüner et al., 2018) and proteins (Liu and Peng, 2017; Wangoo et al., 2008), increasing their internalization and biocompatibility, as well as bounding to antibodies linked to specific cell receptors that have an overexpression in tumor cells (Popovter et al, 2011; Hainfeld et al, 2011), allowing to incorporate in a higher concentration inside malignant cells versus healthy tissue cells (Ahn et al., 2013; Hainfeld et al., 2013, 2006).

These improvement achieved in the generation of high specificity biomolecules decorated-nanoparticles, have motivated nanoparticles future use for small clusters of cancer cells detection (not allowed by traditional contrast image agents) or to provide tumor characteristics information like distribution and radiosensitivity of the tumor cells (by supplying simultaneously different nanoparticles decorated with biomarkers associated with each tumor characteristics) allowing to generate multiparametric images and produce personalized cancer therapy regimes (Ricketts et al., 2012).

Different X-ray techniques has been proposed to identify and quantify high Z nanoparticles allowing different detection limits and sensibility. The most studied techniques were conventional computed tomography (CT) and micro-CT systems (Hainfeld et al., 2011, 2010; Popovtzer et al., 2008). However, CT and micro-CT techniques do not allow simultaneous distinction among different types of nanoparticles embedded in the tumor. Energy Dispersive X-ray Fluorescence (EDXRF) is an effective, fast and non-destructive multielemental technique to determine trace elements in different types of samples offering advantages compared to devices based only on the incident beam attenuation. Several experimental setups have been evaluated for quantification of gold and silver nanoparticles by bench-top EDXRF systems, using both L and K lines for the detection, thus achieving different sensitivity ranges and depths (Figueroa et al., 2015; Manohar et al., 2013; Ren et al., 2014; Ricketts et al., 2016, 2013, 2012; Santibáñez et al., 2017; Wu et al., 2013). EDXRF studies enabled multiparametric imaging of each nanoparticle and the possibility of correlating the biomarker adding to the nanoparticle with the specific characteristics of tumor tissues under study (Ricketts et al., 2012, 2013).

One of the common challenges faced, when using these new agents, is the need to develop detection methodologies: in vivo, quick, efficient, with greater sensitivity and lower doses in those cases involving organisms. Optimizing incident spectrum produced by bench-top EDXRF system that efficiently excites nanoparticles of two different elements is an important challenge for implementing future clinical analysis of the tumor characteristic of each patient.

The aim of this work is to characterize an optimized EDXRF system to detect and quantify in vivo lower concentration of GNPs and AgNPs distributed in tissue-equivalent phantom, requiring lowest surface doses to allow this range of sensitivity. System characterization was carried out testing different combinations of filters with different thickness used to hardening the Bremsstrahlung spectrum, thus producing energetically narrow beams with central energy closer to excitation edges Ag-Kα and Au-LIII, improving the sensitivity-doses relationship and using like statistical figure of merit the sensitivity obtained (limit of detection) weighted by the delivered surface doses.

2. Methodology

2.1. Experimental setup

The setup used for gold nanoparticles (GNPs) and silver nanoparticles (AgNPs) detection was mounted in the LIIFAMIR^X beamline (Valente et al., 2016) at FAMAF (Universidad Nacional de Córdoba, Argentina) as depicted in Fig. 1. The essential parts are: 1) A 3 kW Kristallofex X-ray generator with tube voltage of 20-60 kV and tube current of 5-50 mA. The tube is equipped with a tungsten target and a mylar output window of 50 μm thickness. 2) An Amptek X-100 CdTe □/X-ray spectrometer consisting of a cadmium tellurium detector coupled to the DP5 Amptek Digital Pulse Processor MCA and power supplies. The active volume of the detector has an area of 9 mm^2 and a 1000 μm thick with a 100 μm beryllium entrance window. The typical resolution of the detector is 0.530 keV (0.850 keV) full width at half maximum (FWHM) at 14.4 keV (122.0 keV) and the maximum count rate up to 2x10^5 counts per second. 3) A ionization chamber model TN 30013 (PTW, Freiburg, Germany) with a sensitive volume of 0.6 cm^3 connected to an electrometer model UNIDOS E (PTW, Freiburg, Germany), calibrated by standard laboratory for determining absorbed dose in water, exposition and KERMA in air. Dose measurements were carried out with an acrylic cylindrical-shaped (35 mm diameter and 53 mm height) phantom filled with deionized water, as shown in Fig. 1.

The phantom was located at 95 cm from the X-ray source exit window, and jaws-like collimation system placed at 17 cm from the source was used to configure beam size as well as filters' positioning, as depicted in Fig. 1. The detector system was placed at 2.5 cm from the phantom surface aimed at increasing detection solid angle. Phantom alignment was verified using digital radiography acquired with a PaXScan 2020+ (Varian, U.S.) flat panel X-ray detector located behind, as shown in

Fig. 1. With this configuration, the resulting beam spot area was 1.5 cm^2, therefore a complete illumination of the region of interest was assured.

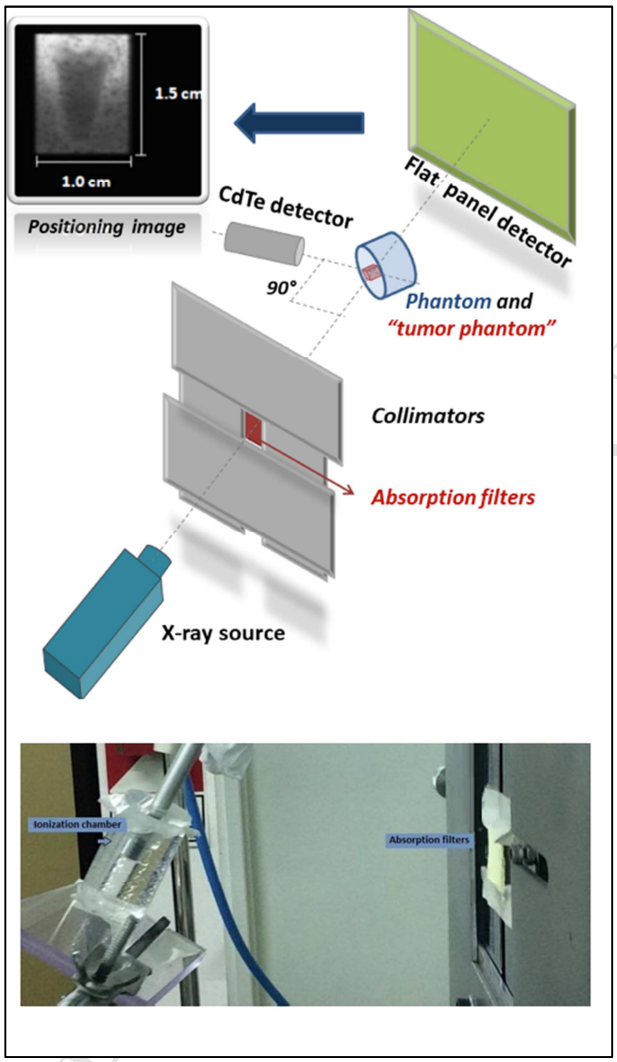

Fig. 1. EDXRF experimental setup for simultaneous gold and silver nanoparticles fluorescence detection (top) and picture of the experimental set up for dosimetry measurements (bottom).

2.2. Sample preparation

An equivalent soft-tissue phantom was prepared using 96% w/w cellulose $(C_6H_{10}O_5)_n$ and 4% w/w of sodium chloride (NaCl), as described elsewhere (Santibáñez et al., 2017), both reactants of analytical grade purchased from Merck (Germany). The phantom is a cylindrical-shaped (35 mm diameter and 30 mm height) having a 0.3 cm^3 cavity to place a "tumor phantom" doped with different concentrations of nanoparticles. The composition of the tumor phantom used to evaluate the different settings consisted of a mixture of 7.500 mg/mL of GNPs (1.9 nm diameter purchased from Aurovist, Nanoprobes Inc., U.S.) and 7.500 mg/mL of AgNPs (8.2±2.0 nm diameter synthesized according to the method developed by (Vedelago et al., 2018)) in deionized water, obtaining concentrations ranging

from 0.010 mg/mL to 7.500 mg/mL. Concentration uncertainties were estimated to be less than 12% for lower concentrations and around 3% for the higher concentrations. Fig. 2 shows a picture of the "tumor phantom" for different nanoparticles concentrations.

Fig. 2. Tumor phantoms with different GNPs and AgNPs concentrations ranging from 0.010 to 7.500 mg/mL.

2.3. Optimized spectrum by suitable filtering and assessment of limit of detection

To assess the optimal incident spectrum for the simultaneous detection of gold and silver nanoparticles in tumor phantom, different combinations of filters were used to configure the X-ray beam. The effect of including absorption filters made of different elements was to increment the relative quantity of photons with energy enough to excite the gold L_{III}-edge (11.9 keV), such as strontium (Sr) and yttrium (Y). Aiming to produce the analogue effect for silver K-edge (25.5 keV), a tin (Sn) was used. Absorption filters were purchased from (EXAFS Materials, Danville, CA 94526 USA).

After beam hardening, the obtained spectra resulted as two energetically narrow beams centered on the specific excitation energy slightly above each edge. Fig. 3 shows two spectra optimized in terms of the capability of simultaneous excitation of Au L_{III} and Ag K lines: "Spectrum A" obtained using 212.0 µm Sr and 94.5 µm Sn filters, and "Spectrum B" obtained using 130.2 µm Y and 94.5 µm Sn filters. For these measurements, all spectra were configured setting current tube at 20 mA and 35 kV voltage during 120 s acquisition time. Additionally, measurements were performed using only one filter with the aim of further comparisons in terms of sensitivity and absorbed dose for cases of a filtering devoted to simultaneous optimization of GNPs ("Spectrum C") and AgNPs ("Spectrum D"). The information of which filter was used for each spectrum was summarized in Table 1 and measured spectra are depicted in Fig. 3.

The statistical figures of merit used for evaluating the optimal spectrum in terms of increasing sensitivity while reducing radiation dose were evaluated as the limit of detection (*LoD*) and the

absorbed dose required for achieving certain level of sensitivity. The *LoD* was calculated using one of the most applied definitions, given by (Van Grieken and Markowicz, 2002):

$$\square\square\square = \frac{3\sqrt{\square_{\square}}}{\square_{\square}}\square \quad (1)$$

where I_B stands for background counts, I_F stand for the fluorescent signal counts and C represents the nanoparticles concentration in the sample. Additionally, the *LoD* values were weighted by a factor that equals the resulting dose from using each spectrum to achieve the same *LoD*, considering that *LoD* is inversely proportional to the square root of the detection time (Santibáñez et al., 2016; Santibáñez et al., 2017).

Table 1. Set of filters used for X-ray spectrum modification.

Detection	Spectrum ID	Configuration of filters
Simultaneous	Spectrum A	Sr (212.0 µm) and Sn (94.5 µm)
	Spectrum B	Y (130.2 µm) and Sn (94.5 µm)
Single	Spectrum C	Y (130.2 µm)
	Spectrum D	Sn (94.5 µm)

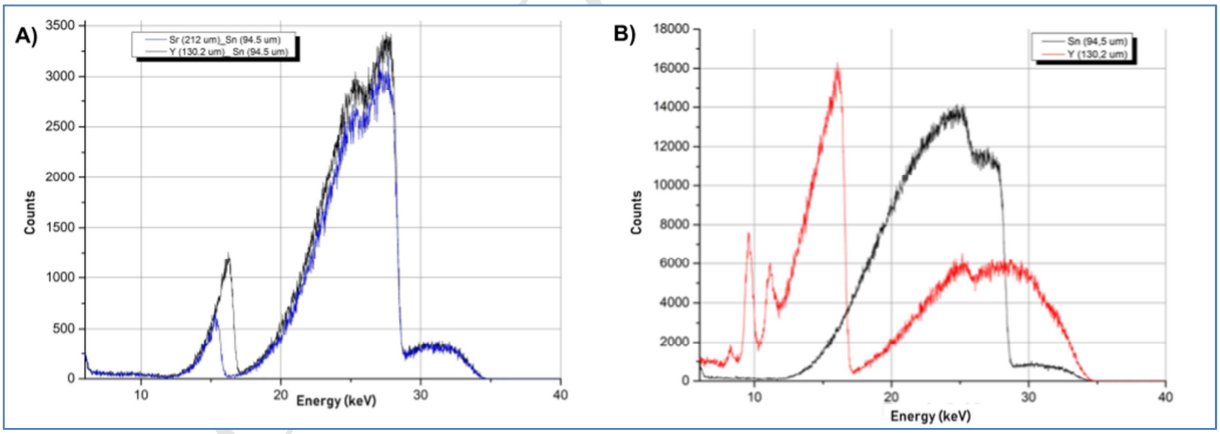

Fig. 3. A) Optimized spectra obtained by combining different filters: Spectrum A (blue line) obtained using 212 µm Sr with 94.5 µm Sn filters and Spectrum B (black line) obtained using 130.2 µm Y with 94.5 µm Sn. B) Single element XRF detection: Spectrum C obtained with 130.2 µm Y filter (red line) and Spectrum D obtained with 94.5 µm Sn filter (black line).

The evaluation of the *LoD* for simultaneous detection was carried out by corresponding response curves of the fluorescent signal as a function of the concentration for each nanoparticle type. Acquisition time was fixed to deliver 0.250 mGy to the phantom considering concentrations of each nanoparticle type for the tumor phantom ranging from 0.010 to 7.500 mg/mL. Additionally, the *LoD*

achieved by the configurations for individual samples consisting of pure Au or Ag nanoparticles were evaluated for further comparison purposes.

On the other hand, evaluation of absorbed dose corresponding to a fixed *LoD* of 0.100 mg/mL for samples made of GNPs and AgNPs. The improvement in the dose necessary for obtain a fixed sensitivity, using as figure of merits the feasibility of obtaining a *LoD* of 0.100 mg/mL of gold and silver nanoparticles in a sample prepared with a concentration of 5.000 mg/mL of Au and Ag nanoparticles (correspond to a signal-to-noise ratio of 150 in an exploratory examination), was evaluated using spectra depicted in Table 1.

The evaluation of the *LoD* of the simultaneous detection was carried out by calibration curves of the fluorescent signal as a function of the concentration of each nanoparticle type. Fluorescent signal intensity was calculated by background subtraction of the corresponding spectrum of the tumor phantom filled with deionized water. Acquisition time was fixed to deliver 0.250 mGy to the phantom considering concentrations of each nanoparticle type for the tumor phantom ranging from 0.010 to 7.500 mg/mL. Additionally, the detection limit achieved by the configurations for single element measurement of Au and Ag nanoparticles, were evaluated for further comparison purposes.

3. Results and discussions

All filtering configurations were measured to determine which one has the highest sensitivity at the lowest radiation dose for simultaneous detection of silver K alpha and gold L alpha fluorescent emissions. The configurations for simultaneous gold and silver fluorescence detection lead to similar results but Spectrum B conduce to higher sensitivity in gold fluorescence detection. Obtained *LoD* values, weighted *LoD* and absorbed dose are reported in Table 2 along with the obtained results for each individual filter. As can be observed, weighted *LoD* are 2% (5%) of the individual detection of gold (silver) fluorescence for Spectrum A and 5% (5%) of the individual detection of gold (silver) fluorescence for Spectrum B, indicating a significant improvement in minimum detectable concentrations and lower dose levels.

The similarity in the results obtained for the detection of silver nanoparticles, versus the clear difference achieved by one of the configurations in the detection of gold nanoparticles, can be explained by observing the incident spectrum in both configurations in Fig. 3. For the spectral region associated with the excitation of gold L line, it is observed that the closest proximity of the K-absorption edge of the strontium (Spectrum A) to the L_{III} absorption edge of gold, results in a narrow beam with energies with a higher probability of producing photoelectric than Spectrum B with the yttrium filter. However, filter's density and thickness determines a greater or lesser fluence in each beam, being higher the production by the configuration of filters in Spectrum B, with the same

acquisition time. The competition of these factors determines that the configuration of Spectrum A achieves a lower *LoD* for gold fluorescent detection, with a similar dose within the error to that produced by Spectrum B configuration.

Table 2. *LoD* obtained for each nanoparticle contrast among with dose values and resulting weighted *LoD*.

Detection	Spectrum ID	*LoD* [mg/mL]	Weighted *LoD* [a.u.]	Dose [mGy]
Simultaneous	Spectrum A	0.140 (Au) 0.476 (Ag)	0.028 (Au) 0.102 (Ag)	0.045±0.002
	Spectrum B	0.315 (Au) 0.450 (Ag)	0.073 (Au) 0.097 (Ag)	0.048±0.002
Single	Spectrum C	0.095 (Au)	1.400 (Au)	0.385±0.009
	Spectrum D	0.286 (Ag)	1.936 (Ag)	0.260±0.008

Apart from that, when analyzing the spectral region associated with the silver K-edge absorption energy, since both configurations of Spectrum A and B uses the same Sn filter, resulting spectra has the same a spectrally narrow beam centered at around 27.5 keV and with a slightly different relative fluence.

The results obtained in the experiments carried out with a fixed *LoD* of 0.100 mg/mL are depicted in Table 3. Comparing dose values required for simultaneous detection of both nanoparticle agents with dose values of the independent measurements of each agent, it was possible to reach sensitivity detection levels 2.24 times lower for Spectrum A and 2.36 times lower for Spectrum B. The configuration of Spectrum B achieves the same *LoD* with a mean dose value smaller but undistinguished within the uncertainty than the one obtained with Spectrum A. Although detection times are 2.48 times higher for Spectrum A and 2.22 times higher for Spectrum B compared to single element fluorescent detection, there are still reasonable times for *in vivo* applications.

Table 3. Time and dose required to obtain a *LoD* of 0.100 mg/mL with the optimized configurations of filters for simultaneously GNPs and AgNPs fluorescent detection, among with single GNPs and AgNPs fluorescent.

Detection	Spectrum ID	Time [s]	Dose [mGy]
Simultaneous	Spectrum A	681	1.02±0.03
	Spectrum B	608	0.97±0.03
Single	Spectrum C	28	0.16±0.01
	Spectrum D	246	2.13±0.05
	Total:	274	2.29±0.06

Measured fluorescence signal intensity for different nanoparticles contrast agent concentrations are depicted in Fig. 4 for Spectrum A and in Fig. 5 for Spectrum B, where each tumor phantom was constituted by both silver and gold nanoparticles. What is more, obtained results for individual element XRF detection are depicted in Fig. 6. Each curve has an inset graphic for the lower concentrations and the resulting detection limit is marked as a red-color area, determined by the intersection of the weighted linear least-squares fit and the value produced by 1.96σ of the blank sample.

For simultaneous detection using Spectrum A, obtained *LoD* are 0.043 mg/mL for gold and 0.019 mg/mL for silver. For simultaneous detection using Spectrum B, obtained *LoD* are 0.044 mg/mL for gold and 0.029 mg/mL for silver. Furthermore, gold XRF single detection reaches a *LoD* of 0.058 mg/mL and silver XRF single detection 0.124 mg/mL. Even though only one filter was used for each element XRF single detection, higher dose values are involved, therefore reducing acquisition time in order to preserve the 0.25 mGy accumulated dose during spectra acquisition.

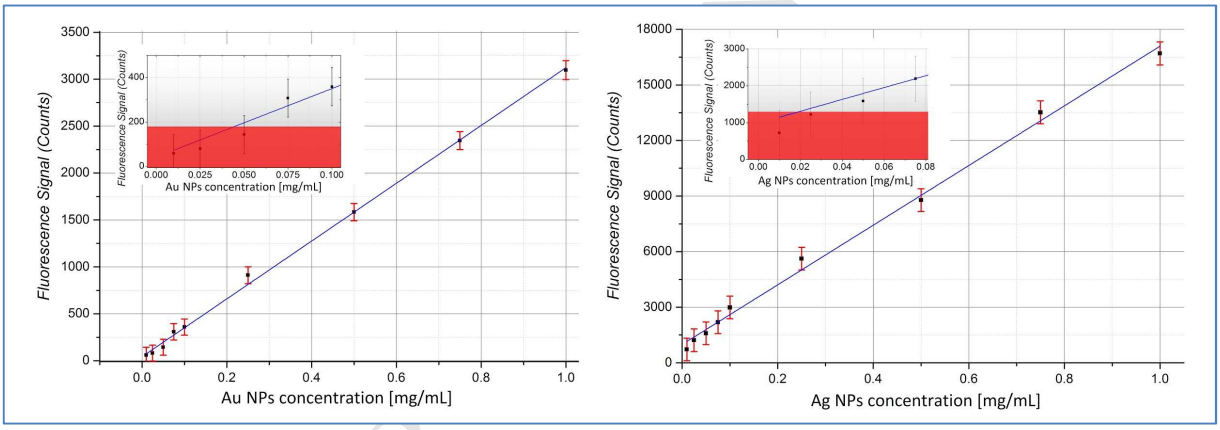

Fig 4. Calibration curve of gold L alpha XRF signal (left) and silver K alpha XRF signal (right) versus the NPs concentration of the tumor phantom for Spectrum A (Sr and Sn filters).

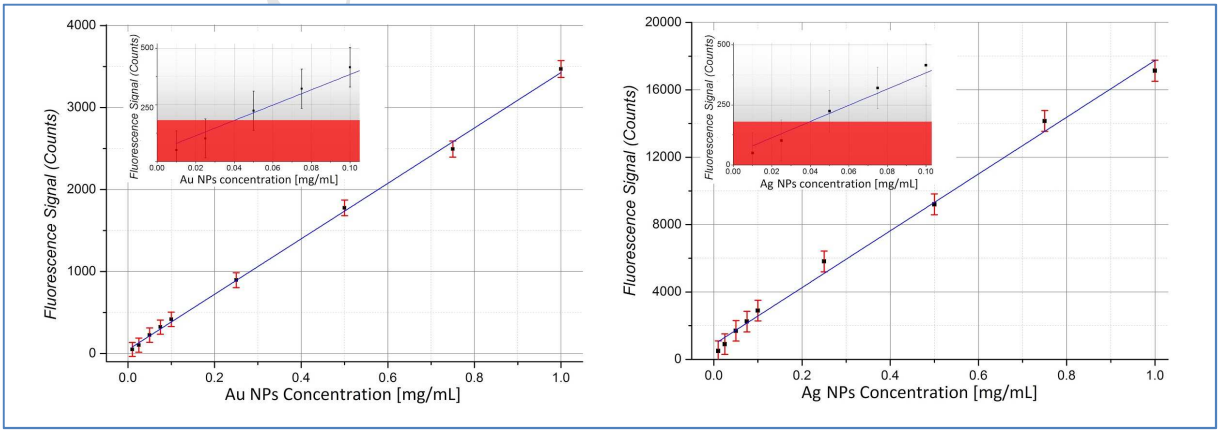

Fig 5. Calibration curve of gold L alpha XRF signal (left) and silver K alpha XRF signal (right) versus the NPs concentration of the tumor phantom for Spectrum B (Y and Sn filters).

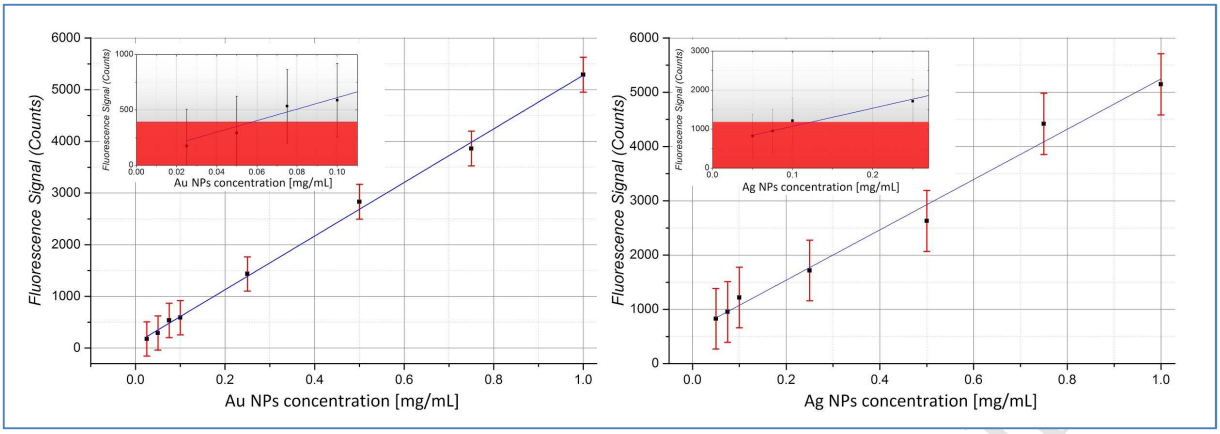

Fig 6. Calibration curve of gold L alpha XRF signal (left) and silver K alpha XRF signal (right) versus the NPs concentration of the tumor phantom for single element detection using Spectrum C for gold and Spectrum D for silver.

Reported *LoD* for simultaneous gold and silver XRF detection were obtained using acquisition times to deliver a 0.250 mGy radiation dose to the tumor, value 40 times less than the 10 mGy value typically recommended for *in vivo* human X-ray analysis (Wielopolski, 1999), therefore the developed technique is in accordance with the "As Low As Reasonably Possible" (ALARA) principle. Because the present work is one of the first to perform a characterization of an optimized EDXRF system for simultaneous XRF detection of gold and silver nanoparticles agents, it has not been reported detection limit values so far that allow a comparison with the obtained results. In the case of single detection of gold XRF, previous work has reported a detection limit of 0.010 mg/mL for Au with benchtop X-ray devices (Ricketts et al., 2013), although using longer acquisition times and the dose administered by the system has not been reported.

4. Conclusions

High sensitivity and low administered radiation dose was achieved by using combinations of absorption filters of different composition and thickness at the output of the X-ray beam to obtained two spectrally narrow beams that efficiently excite the gold L_{III}-edge and silver K-edge, respectively. The limit of detection achieved with these configurations was more than two times lower for both tested configurations when compared to the individual detection of the agents studied, mainly due to the shorter acquisition times used for single gold or silver fluorescent detection.

To the best of author's knowledge, it was possible to configure for the first time an X-ray fluorescence system that would allow the simultaneously *in vivo* detection and quantification of gold and silver nanoparticle agents, that may have certain characteristics necessary for future clinical *in vivo* applications. Specifically, one of the characteristics achieved was to obtain a high sensitivity

EDXRF system for the detection of the studied agents, close to the expected values of the concentrations found *in vivo* in the tumor. In addition, due to the application of ionizing radiation in humans, optimizations were made to reduce applied radiation dose, achieving values 40 times less than the ones usually recommended for *in vivo* X-ray applications.

Acknowledgments

This work has been supported by the Universidad de La Frontera through DIUFRO grant DI19-1005 and by CONICYT program through FONDECYT grant No. 11150673. Authors R. Saavedra would like to thanks CONICYT for scholarship No. 22151920.

References

Ahn, S., Jung, S.Y., Lee, S.J. (2013). Molecules, 18, 5858-5890.

Albertini, B., Mathieu, V., Iraci, N., Van Woensel, M., Schoubben, A., Donnadio, A., Greco, S., Ricci, M., Temperini, A., Blasi, P., Wauthoz, N. (2019). Molecular Pharmaceutics. 16, 2430-2444.

Bromma, K., Rieck, K., Kulkarni, J., O'Sullivan C., Sung, W., Cullis, P., Schuemann, J. 2019. Cancer Nano. 10: 1.

Chen, G., Xie, Y., Peltier, R., Lei, H., Wang, P., Chen, J., Hu, Y., Wang, F., Yao, X., Sun, H. 2016. ACS Applied Materials & Interfaces. 8, 11204-11209.

Cheong, B., Jones, A., Siddiqi, F., Liu, N., Manohar, M., Cho, S., 2010. Phys. Med. Biol. 55, 647-662.

Delorme, R., taupin, F., flaender, M., ravanat, J.L., champion, Ch., agelou, M., elleaume, H., 2017.

Figueroa, R.G., Santibañez, M., Valdez, C.N., Valente, M., 2015. Radiat. Phys. Chem. 117, 198-202.

Grüner, F., Blumendorf, F., Schmutzler, O., Staufer, T., Bradbury, M., Wiesner, U., Hoeschen, C. 2018. Scientific reports, 8, 16561.

Hainfeld, J.F., Slatkin, D.N., Focella, T.M., Smilowitz, H.M., 2006. Br. J. Radiol. 79, 248-253.

Hainfeld, J.F., Dilmanian, F.A., Zhong, Z., Slatkin, D.N., Kalef-Ezra, J.A., Smilowitz, H.M., 2010. Phys. Med. Biol. 55, 3045-3059.

Hainfeld, J.F., O'Connor, M.J., Dilmanian, F.A., Slatkin, D.N., Adams, D.J., Smlowitz, H.M., 2011. Br. J. Radiol. 84, 526-533.

Hainfeld, J.F., Smilowitz, H.M., O'Connor, M.J., Dilmanian, F.A., Slatkin, D.N., 2013. Nanomedicine 8, 1601-1609.

Liu, J. Peng, Q. (2017). Acta Biomater. 55:13-27.

Manohar, N., Reynoso, F., Cho, S., 2013. Med. Phys. 40, 080702.

Mattea, F., Vedelago, J., Malano, F., Gomez, C., Strumia, M.C., Valente, M., (2017). Radiat. Phys. Chem. 130, 442-450.

Ngwa, W., Kumar, R., Sridhar, S., Korideck, H., Zygmanski, P., Cormack, R.A., Berbeco, R., Makrigiorgos, M., (2014). Nanomedicine 9, 1063-1082.

Popovtzer, R., Agrawal, A., Kotov, N.A., Popovtzer, A., Balter, J., Carey, T.E., Kopelman, R., 2008. Nano Lett. 8, 4593-4596.

Popovtzer R. (2011). Int J Nanomedicine. 6, 2859.

Ren, L., Wu, D., Li, Y., Wang, G., Wu, X., Liu, H., 2014. Med. Phys. 41, 031902.

Ricketts, K., Castoldi, A., Guazzoni, C., Ozkan, C., Christodoulou, C., Gibson, A.P., Royle, G.J., 2012. Phys. Med. Biol. 57, 5543–5555.

Ricketts, K., Guazzoni, C., Castoldi, A., Gibson, A.P., Royle, G.J., 2013. Phys. Med. Biol. 58, 7841-7855.

Ricketts, K., Guazzoni, C., Castoldi, A., Royle, G., 2016. Nucl. Instrum. Methods Phys. Res. A. 816, 25-32.

Santibañez, M., Vásquez, M., Figueroa, R.G., Valente, M., 2016. Radiat. Phys. Chem. 122, 28-34.

Santibáñez, M., Saavedra, R., Vásqueza, M., Malano, F., Pérez, P., Valente, M., Figueroa, R.G., 2017. Appl. Radiat. Isot. 129, 19-27.

Santibáñez, M., Guillen, Y., Chacón, D., Figueroa, R.G., Valente, M. 2018. Appl. Radiat. Isot. 141, 210-218

Wangoo, N., Bhasin, K.K., Mehta, S.K., Suri, C.R. (2008). J. Colloid Interface Sci. 2008, 323, 247-54.

Wu, D., Li, Y., Wong, M.D., Liu, H., 2013. Med. Phys. 40, 051901.

Valente, M., Graña, D., Malano, F., Perez, P., Quintana C., Tirao G., Vedelago J., 2016. IEEE Lat. Am. T. 14(9), 3967-3973.

Van Grieken, R., Markowicz, A., 2002. Handbook of X-ray Spectrometry, 2nd ed. Marcel Dekker, New York.

Vedelago, J., Gomez, C.G., Valente, M., Mattea, F.2018, Radiation Physics and Chemistry 146, 55-67.

Wielopolski, L. (1999). Adv. X-Ray Anal, 41(892-897), 0376-0308.

Yang. C., Bromma, K., Chithrani, B.D. (2018). Cancers. 10:84. Hainfeld, J.F., Slatkin, D.N., Smilowitz, H.M., 2004. Phys. Med. Biol. 49, 309-315.

Zhang, D.G., Feygelman, V., Moros, E.G., Latifi, K., Zhang, G.G., 2014. PLoS One 9, e109389.

(FIGURE 1)

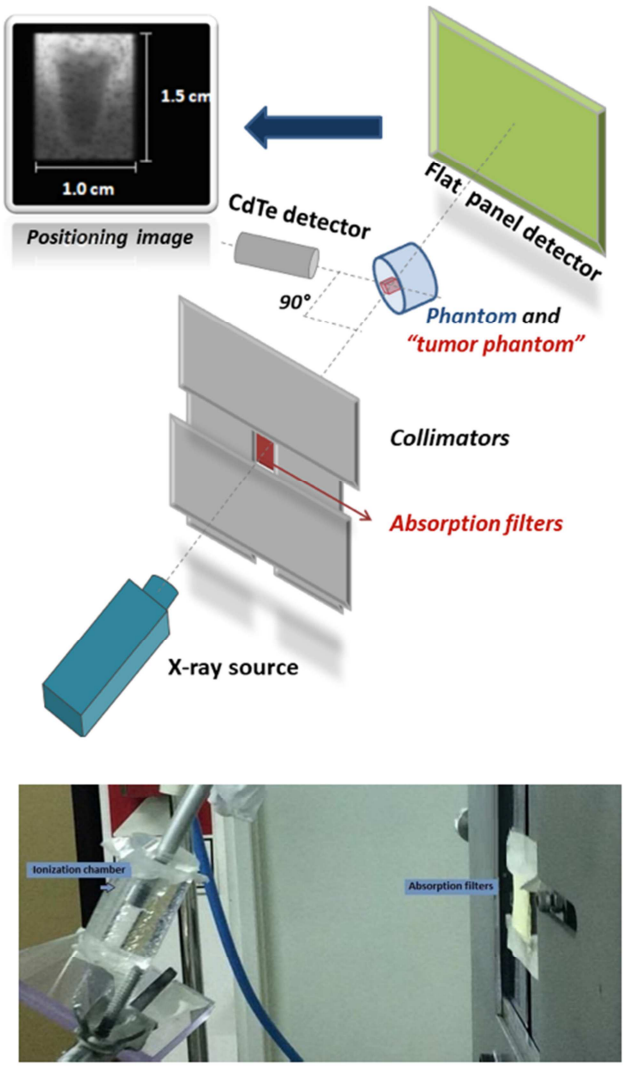

Caption to figure 1:

EDXRF experimental setup for simultaneous gold and silver nanoparticles fluorescence detection (top) and picture of the experimental set up for dosimetry measurements (bottom).

(FIGURE 2)

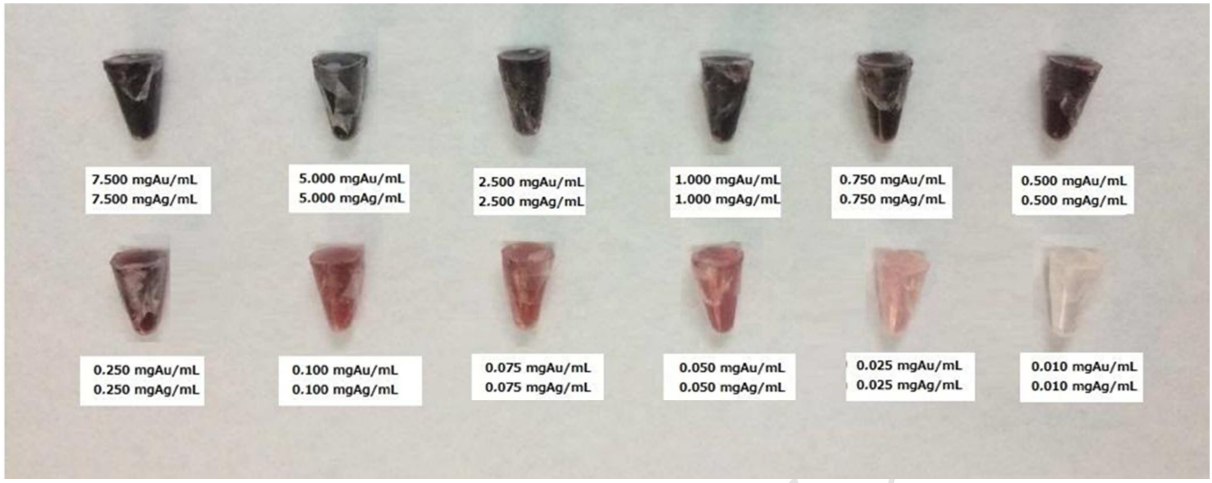

Caption to figure 2:

Tumor phantoms with different GNPs and AgNPs concentrations ranging from 0.010 to 7.500 mg/mL.

(FIGURE 3)

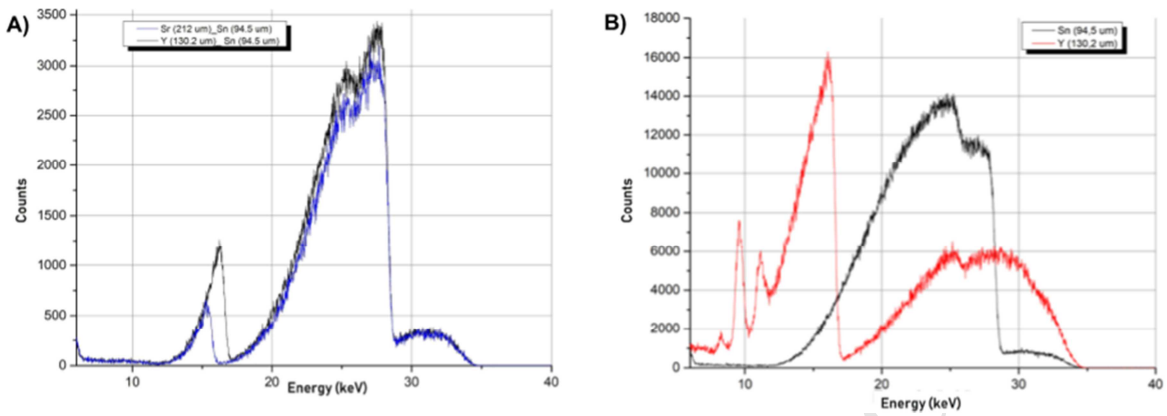

Caption to Figure 3:

A) Optimized spectra obtained by combining different filters: Spectrum A (blue line) obtained using 212 µm Sr with 94.5 µm Sn filters and Spectrum B (black line) obtained using 130.2 µm Y with 94.5 µm Sn. B) Single element XRF detection: Spectrum C obtained with 130.2 µm Y filter (red line) and Spectrum D obtained with 94.5 µm Sn filter (black line).

(FIGURE 4)

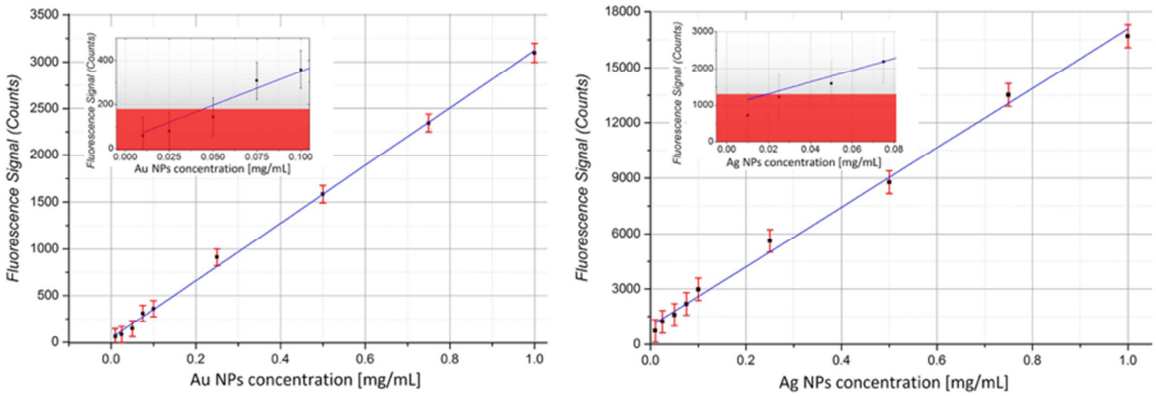

Caption to Figure 4:

Calibration curve of gold L alpha XRF signal (left) and silver K alpha XRF signal (right) versus the NPs concentration of the tumor phantom for Spectrum A (Sr and Sn filters).

(FIGURE 5)

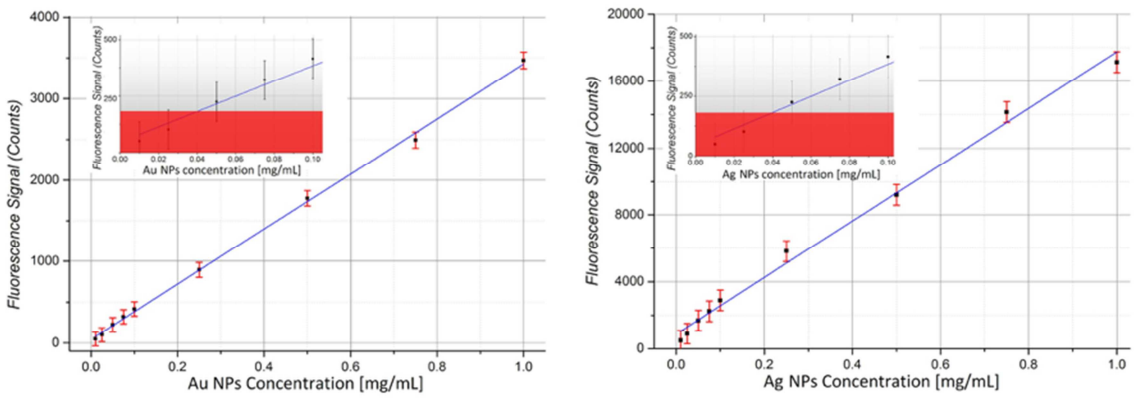

Caption to Figure 5:

Calibration curve of gold L alpha XRF signal (left) and silver K alpha XRF signal (right) versus the NPs concentration of the tumor phantom for Spectrum B (Y and Sn filters).

(FIGURE 6)

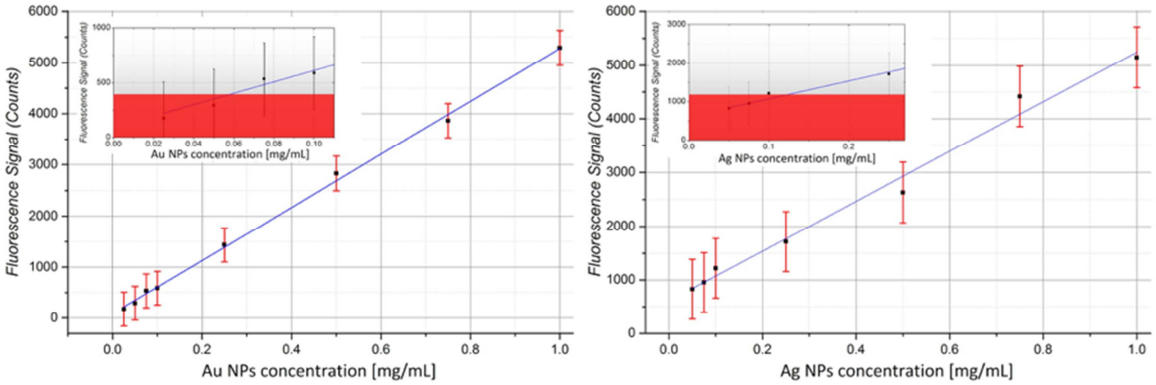

Caption to Figure 6:

Calibration curve of gold L alpha XRF signal (left) and silver K alpha XRF signal (right) versus the NPs concentration of the tumor phantom for single element detection using Spectrum C for gold and Spectrum D for silver.

HIGHLIGHTS

- Optimized XRF simultaneous detection of Au and Ag nanoparticles in water-like phantoms.
- Simultaneous detection can be suitably optimized by incident spectrum configuration.
- Potentiality of simultaneous high Z agents' detection for theranostics.